Rapid Communications

Electrical control of excitons in van der Waals heterostructures with type-II band alignment

A. Chaves,[1,*] J. G. Azadani,[2] V. Ongun Özçelik,[3] R. Grassi,[2] and T. Low[2,†]

[1]*Departamento de Física, Universidade Federal do Ceará, Caixa Postal 6030, Campus do Pici, 60455-900 Fortaleza, Ceará, Brazil*

[2]*Department of Electrical and Computer Engineering, University of Minnesota, Minneapolis, Minnesota 55455, USA*

[3]*Andlinger Center for Energy and the Environment, Princeton University, Princeton, New Jersey 08544, USA*

(Received 15 September 2017; revised manuscript received 6 June 2018; published 12 September 2018)

We investigate excitons in stacked transition-metal dichalcogenide layers under a perpendicularly applied electric field, herein $MoSe_2/WSe_2$ van der Waals heterostructures (vdWHs). Band structures are obtained with density functional theory (DFT), along with electron and hole wave functions in conduction and valence bands, respectively. A minimal continuum model, parametrized by the DFT results, is presented, allowing for the calculation of the excitonic states. Although the type-II nature of the heterostructure leads to a fully charge separated interlayer exciton on the ground states, our results show that moderate values of electric field produce more evenly distributed wave functions along the vdWH, namely, hybrid inter/intralayer exciton states, where both the interlayer exciton binding energy and, most notably, its oscillator strength are enhanced.

DOI: 10.1103/PhysRevB.98.121302

Introduction. Recent experimental and theoretical analyses of transition-metal dichalcogenides (TMDCs) have demonstrated that these indirect gap materials, when exfoliated into their monolayer form, acquire a direct gap at the K point of the Brillouin zone edge [1–8]. Across the different types of transition-metal and chalcogen combinations, surveys of their optical gap [9–14], excitonic Rydberg spectra [15,16], and trion and biexciton formation [17–19] provide evidence of strong electron-hole (e-h) interactions, due to the reduced dielectric screening in these systems. van der Waals heterostructures (vdWHs), through either vertical stacks or lateral attachment of different materials, present a promising avenue to engineering excitonic properties. Several experimental groups have reported advances in this direction, particularly on the investigation of photoluminescence (PL) in vertically stacked vdWH bilayers [20–26].

Recent efforts on vdWHs have been focused on the pursuit for experimental evidence of spatially indirect interlayer excitons (ILEs), i.e., where the electron and hole forming the excitonic pair are confined at different materials. This situation is expected to occur in combinations of TMDCs with type-II band alignment [27], i.e., both the conduction and valence band of one layer are at a higher energy as compared to the same bands in the other layer. Such a spatially separated e-h pair should in general have a very small e-h overlap and, consequently, a longer recombination time, or exciton lifetime. This could potentially be of interest for energy storage and photodetector applications, where long exciton lifetimes are required [28]. However, ILE has been proven to be elusive in experiments, since its very low oscillator strength forbids an interlayer valence-to-conduction band transition to occur in light absorption measurements.

Here, we investigate the electronic and excitonic properties of a prototypical type-II vdWH, namely, $MoSe_2/WSe_2$, under a perpendicular electric field. Our results reveal strong electrical control of the exciton binding energies and its oscillator strength. The former and latter would dictate the PL spectral resonance position and intensity, respectively. Electronic band structures are obtained using density functional theory (DFT) calculations, whereas excitonic states are described within the Wannier-Mott approach [29,30]. In the absence of electric field, quasiparticle states around the K point are shown to be fully charge separated between the layers, due to the type-II band mismatch, thus forming a vertical intrinsic electric dipole. As the field is applied opposite to the dipole direction, it pushes single electron and hole states towards each other across the bilayer, forcing the dipole to flip. At the crossover electric field, the dipole moment is minimized. In this case, the interlayer exciton oscillator strength and binding energies are shown to attain maximum values, which suggests, e.g., the possibility of observing a higher ILE peak and a visible blueshift of its position in PL experiments. The application of such an intermediate field can be achieved either by gating or doping one of the layers. The possibility of having a reciprocal space indirect interlayer conduction-to-valence band transition (between the K and Γ points) is also discussed. Results discussed here are expected to be applicable to other type-II combinations of Mo- and W-based diselenides and disulfides.

Theoretical model. In order to obtain the band structure and electron/hole distributions for the vdWH, DFT calculations were performed using the Vienna *ab initio* simulation package (VASP) [31]. We used projector augmented-wave (PAW) [32] potentials and approximated the exchange-correlation potential with the Perdew-Burke-Ernzerhof (PBE+D2) functionals [33,34]. van der Waals corrections [34] and spin-orbit coupling were included in the calculations. During the ionic relaxation, the Brillouin zone of the unit cell was sampled by a grid of $(17 \times 17 \times 1)$ k points. A plane-wave basis set with an energy cutoff of 400 eV was used in all calculations. A

*andrey@fisica.ufc.br
†tlow@umn.edu

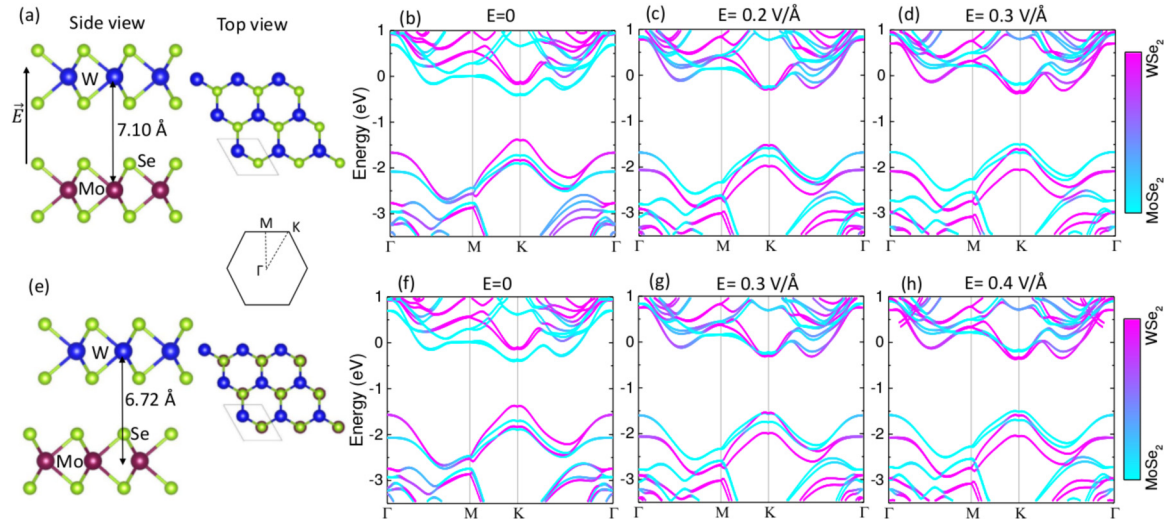

FIG. 1. Side and top views of the crystal structure of a $MoSe_2/WSe_2$ heterostructure with (a) AA and (e) AA' stacking orientation. Notice the red (Mo) atoms below the green (Se) ones in the AA' case (e). Inset: First Brillouin zone and its high symmetry points. The in-plane lattice constant a is 3.33 Å, the Mo-Se distance is 2.54 Å, while interlayer distances are 7.10 and 6.72 Å for the AA and AA' cases, respectively. The vertical arrow illustrates the positive direction of applied electric field $\vec{E}$. Band structures of an AA stacked $MoSe_2/WSe_2$ heterostructure (b) without applied electric field, and with applied fields (c) $E = 0.2$ V/Å and (d) $E = 0.3$ V/Å are shown. (f)–(h) The same as (b)–(d), but for AA' stacking and $E = 0.3$ V/Å and $E = 0.4$ V/Å. The color scale indicates the relative wave-function projections to the $MoSe_2$ (blue) and WSe_2 (pink) layers.

large out-of-plane supercell size of 36 Å (25 Å vacuum separation) was chosen to ensure no interaction between adjacent supercells. While applying an external electric field, dipole corrections were applied in order to remove spurious dipole interactions [35].

In general, TMDC bilayers are shown to be indirect gap semiconductors [1,2]. However, recently synthesized vdWH with AA stacking, instead of the natural AB case, exhibit a direct gap at K [25]. Electronically, these two layers are largely decoupled, with a superposition of their monolayers' band structure. Alternatively, AA' stacked bilayers, namely, with transition-metal atoms of one layer superposing chalcogen atoms of the other layer, also share the same qualitative features. In our calculations, the geometry of AA and AA' stacked $MoSe_2/WSe_2$ supercells was first optimized at zero electric field, leading to the crystal structures shown in Figs. 1(a) and 1(e). For any other value of perpendicular electric field, we computed the optimum interlayer distance, by allowing the ions to relax in the out-of-plane direction until the atomic forces on the unit cell were less than 0.01 eV/Å, all obtained without spin-orbit coupling. The charge density was computed by refining the solution to the Kohn-Sham equations with an energy convergence value of 10^{-5} eV. Energies in all DFT results throughout this Rapid Communication are shown using vacuum energy at zero electric field as a reference.

From the pseudowave function $\Psi_{n,\vec{k}}(\vec{r}) = [\psi^{\uparrow}_{n,\vec{k}}(\vec{r}), \psi^{\downarrow}_{n,\vec{k}}(\vec{r})]^T$ of a specific band n and $\vec{k}$ point (in what follows, we choose either $\vec{k} = K$ or $\vec{k} = \Gamma$), we extracted the probability function projection [36] to the bottom (top) $MoSe_2$ (WSe_2) layer as

$$\Phi^{(n)}_{1(2)} = \int_{z_{\min}(z_0)}^{z_0(z_{\max})} dz \int_{\Omega_{2D}} dx\, dy [|\psi^{\uparrow}_{n,\vec{k}}(\vec{r})|^2 + |\psi^{\downarrow}_{n,\vec{k}}(\vec{r})|^2], \tag{1}$$

where Ω_{2D} stands for the two-dimensional Wigner-Seitz cell, $z_{\min}$ and $z_{\max}$ are the supercell lower and upper boundaries in the out-of-plane direction, respectively, and z_0 is the midpoint position between the two layers.

The exciton wave function is defined in the basis $[\Psi_{11}(\rho)\ \Psi_{12}(\rho)\ \Psi_{21}(\rho)\ \Psi_{22}(\rho)]^T$, where $\vec{\rho} = \vec{\rho}_e - \vec{\rho}_h$ is the electron-hole relative coordinate, i (j) denotes an electron (hole) in the $i(j)$th layer, and $i, j = 1(2)$ stands for the bottom (top) layer. The exciton Hamiltonian reads [37–39]

$$H_{\text{exc}} = \begin{pmatrix} H_{11} + V_h & t_h & t_e & 0 \\ t_h^* & H_{12} - PE & 0 & t_e \\ t_e^* & 0 & H_{21} + V_h + V_e + PE & t_h \\ 0 & t_e^* & t_h^* & H_{22} + V_e \end{pmatrix}, \tag{2}$$

where E is the field intensity, P is the effective dipole moment in the direction perpendicular to the vdWH, $H_{ij} = (1/\mu^{ij})\nabla^2_{\parallel} + V_{ij}(\rho)$, μ_{ij} is the reduced effective mass [40] for an electron (hole) in the $i(j)$th layer, and the e-h interaction

potential $V_{ij}(\rho)$ is obtained from the quantum electrostatic heterostructure model [41,42]. The interlayer hopping parameters $t_{e(h)}$ and band offsets $V_{e(h)}$ in Eq. (2) are adjusted as to fit the quasiparticle probability densities $\Phi^{(n)}_{1(2)}$ obtained from DFT calculations, i.e., without e-h interactions [37]. We numerically solve the Schrödinger equation for the in-plane component of the wave function $H_{ij}\psi_{ij}(\rho) = E^{\parallel}_{ij}\psi_{ij}(\rho)$, yielding $|\Psi_{ij}(\rho)\rangle = \psi_{ij}(\rho)|\phi_{ij}\rangle$, where $|\phi_{ij}\rangle$ carries information only on the particle localization in each layer. The exciton energy states are then finally obtained by diagonalization of the full exciton Hamiltonian matrix $H_{\rm exc}$ in the $|\phi_{ij}\rangle$ basis, using the calculated $H_{ij} \to E^{\parallel}_{ij}$, whereas the binding energy of the nth exciton state $E^{(n)}_b$ ($n = 1$–4) is taken just as a bra-ket of the e-h interaction part of the exciton Hamiltonian [i.e., setting $t_{e(h)}$, $V_{e(h)}$ and P to zero in Eq. (2)] using the nth eigenfunction of $H_{\rm exc}$.

Results. DFT results in Figs. 1(b)–1(d) and 1(f)–1(h) show that the $MoSe_2/WSe_2$ heterostructure is a direct gap semiconductor at the K point under all values of applied electric field investigated here, for both stacking configurations. Figures 1(b) and 1(f) show the band structure of the AA and AA' stacked heterostructures at zero electric field. In both cases, from the color scale, one verifies that the wave functions at the K point are well localized in either the $MoSe_2$ or WSe_2 layer. Hence, the combined band diagram of the heterostructure preserves the properties of the band structure of its constituent monolayers. This observation supports the idea of using the layer-localized states ($|\phi_{ij}\rangle$) as a basis for the effective exciton Hamiltonian in Eq. (2).

When a positive electric field is applied [see Fig. 1(a)], the bands around K with a prevalent $MoSe_2$ (WSe_2) character shift to higher (lower) energies [see Figs. 1(c) and 1(d)]. This eventually results in band anticrossings around 0.2 V/Å. The same situation holds for AA' stacked heterostructures, as shown in Figs. 1(f)–1(h), albeit at a higher crossover electric field of ≈0.3 V/Å instead. A similar effect is also discussed in Ref. [43].

The energies of the two lowest conduction bands and the two highest valence bands at the K point are plotted as a function of electric field in Fig. 2(a). It is clear that the band gap energy of the heterostructure can be modulated by the electric field, reaching its maximum value of 1.28 eV at 0.225 V/Å. The anticrossing observed in each pair of bands exhibits an energy separation of only a few meV, as a consequence of small interlayer hoppings for quasiparticle states at K [37]. For the Γ point, on the other hand, valence band states have highly mixed wave-function projections, with hole states delocalized across both layers. Consequently, valence band extrema at Γ in Fig. 2(b) exhibit an anticrossing at ≈0.185 V/Å with an energy separation of ≈0.4 eV, two orders of magnitude higher than observed for states at K. Similar qualitative features are observed also in the AA' stacking case in Figs. 2(c) and 2(d).

Despite the fact that the valence band maximum is at K, the satellite valley at Γ is very close in energy and might be experimentally accessible as well. In fact, recent PL experiments suggest the observation of momentum-space indirect ILE in similar type-II vdWHs [20,44–46]. Although the indirect ILE case is briefly discussed in the Supplemental Material [37],

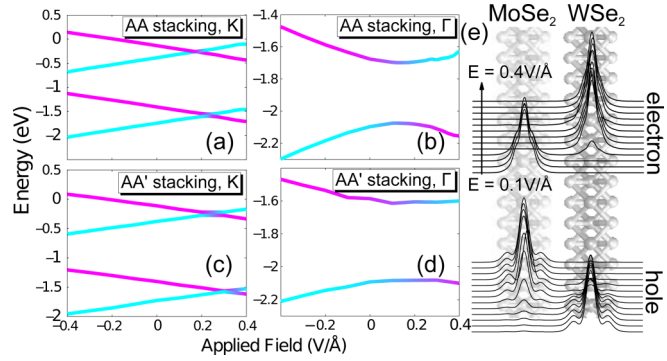

FIG. 2. (a) Two lowest conduction band states and highest valence band states (VBM) for an AA stacked $MoSe_2/WSe_2$ heterostructure under a perpendicularly applied electric field at the K point. (b) Valence band extrema at the Γ point as a function of the electric field. The same results, but for AA' stacking, are shown in (c) and (d), respectively. Color coding is the same as in Fig. 1, thus indicating the relative wave-function projections to the $MoSe_2$ (blue) and WSe_2 (pink) layers. (e) Electron and hole probability densities around the WSe_2 and $MoSe_2$ layers, for different values of applied electric field E, ranging from 0.1 to 0.4 V/Å in steps of 0.025 V/Å.

a proper theoretical investigation of this problem requires taking phonons into consideration, which is beyond the scope of the present work. Therefore, in what follows, valence band states at Γ under applied fields will be discussed only in the quasiparticle level, without e-h interactions.

The DFT obtained probability densities for electron and hole states around K in the AA stacking case are illustrated in Fig. 2(e), for different values of the perpendicularly applied electric field E. For low fields, electrons (holes) are strongly localized in the $MoSe_2$ (WSe_2) layer. As the applied field becomes more positive, charge carriers are pushed towards the opposite layer, and the localization of these particles is interchanged. For intermediate values of the applied field, however, the wave functions partially populate both layers and, consequently, a stronger e-h population overlap is observed, leading to higher binding energies and oscillator strengths, as we will demonstrate further.

Figure 3(a) shows wave-function projections [see Eq. (1)] of the lowest conduction band minimum (CBM) at the K point, for AA stacking (symbols). For electric field values lower than 0.175 V/Å, the wave function is almost completely localized in the first layer ($MoSe_2$). As the applied electric field increases, there is a shift to the other layer (WSe_2). For the valence band maximum (VBM) at K, shown in Fig. 3(b), this trend is reversed, as expected from the type-II band alignment. Besides, the transition is smoother for VBM, indicating a more pronounced band mixing at the band crossing. As for the valence band states at the Γ point in Fig. 3(c), the behavior is almost the same as for the hole states at the K point, but there is an even smoother shift of wave functions from one layer to the other. An intrinsic ≈72%–28% (≈68%–32%) distribution of this wave function between both layers is observed in the absence of an applied field, for the AA (AA') stacking case. Hopping parameters $t_{e(h)}$ in Eq. (2) [for $V_{ij}(\rho) \equiv 0$] are adjusted as to fit the DFT obtained quasiparticle projections

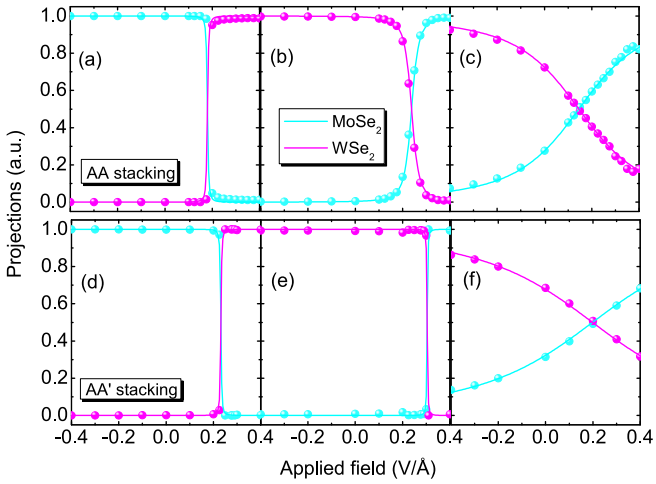

FIG. 3. Normalized wave-function projections on the $MoSe_2$ and WSe_2 layers for (a) CBM and (b) VBM at the K point, as well as for (c) VBM at the Γ point, assuming an AA stacked vdW heterostructure. (d)–(f) The same results, but for the AA' stacking case. Lines and symbols represent results obtained, respectively, from the exciton Hamiltonian matrix in Eq. (2) [in the absence of electron-hole interactions, i.e., for $V_{ij}(\rho) \equiv 0$] and from DFT calculations, according to Eq. (1).

[37], so that good agreement between DFT (symbols) and continuum (lines) model results is achieved in all cases.

Exciton energy states at K are shown in Fig. 4(a) [Fig. 4(c)] for the AA (AA') stacked vdWH. The zero-energy reference is set as the gap between the conduction band edge of $MoSe_2$ and valence band edge of WSe_2. At zero field, a lowest-energy pure ILE state is observed, with a low e-h overlap, at -0.26 eV. Also, the pure intralayer exciton in WSe_2 ($MoSe_2$) peaks at -0.14 eV (0.066 eV), with $E_b^{(2)} \approx 0.39$ eV ($E_b^{(3)} \approx 0.40$ eV) for AA stacking. As the field increases, ILE energy

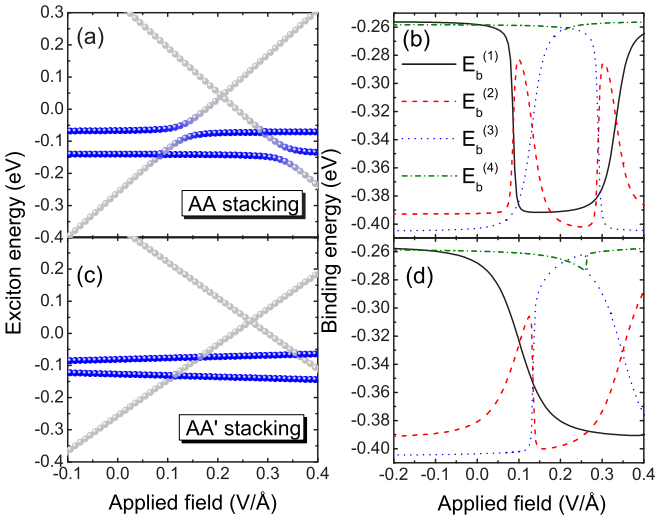

FIG. 4. (a) Exciton energy states $n = 1$–4 and (b) their binding energies $E_b^{(n)}$ as a function of the applied field, assuming AA stacking. The same results are shown in (c) and (d) for the AA' stacking case. Color code in (a) represents the electron-hole overlap from zero (gray) to unity (blue).

exhibits a linear quantum-confined Stark effect, as expected from its nonzero dipole moment parallel to the field, and indeed observed in recent experiments [21,46]. Remarkably, at $E \approx 0.1$ V/Å, the band alignment is so that the conduction band offset approaches zero, while the nonzero t_e enables a state with electrons more evenly distributed among both layers. Consequently, a hybrid state composed of ILE and WSe_2 intralayer excitons is enabled, leading to an anticrossing point in Fig. 4(a) and enhancing the e-h overlap of ILE state in the vicinity of this point. A second (and more clear) anticrossing appears around $E = 0.13$ V/Å, as ILE and $MoSe_2$ intralayer excitons hybridize. The binding energy of the ILE, formerly $E_b^{(1)} \approx 0.26$ eV at $E = 0$ [see Fig. 4(b), solid line], is thus enhanced to $E_b^{(2)} = E_b^{(3)} \approx 0.33$ eV at $E = 0.13$ V/Å. Qualitatively similar features are observed at the other anticrossings for higher fields in Fig. 4(a), as well as for the AA' stacking case [see Figs. 4(c) and 4(d)], although anticrossings in the latter exhibit a very short gap, due to the smaller $t_{e(h)}$ in this case.

According to Elliot's formula [47], the intensity (oscillator strength) of excitonic peaks is proportional to the square modulus of the exciton envelope wave function at $r = 0$, i.e., where electrons and holes are at the same point in space, as well as on the dipole matrix element of the quasiparticle states. The latter depends on the symmetry of the bands, which is not expected to change with the perpendicularly applied field. Moreover, for the AA and AA' stacking considered here, the dipole matrix element is demonstrated to be nonzero, thus allowing for excitonic transitions [48,49]. Therefore, variations in the electron-hole overlap are reflected in the exciton peak intensity [50,51], as experimentally verified [52] in coupled semiconductor quantum wells, which is analogous to the coupled layer case investigated here. Consequently, the effects discussed here would manifest themselves in PL experiments as an ILE peak whose spectral position and amplitude change with external electric field.

Conclusion. We have investigated the exciton states in $MoSe_2/WSe_2$ heterostructures in the presence of an electric field applied perpendicularly to the layers. For almost any value of field, this heterostructure exhibits type-II band offsets for states around the K point of the Brillouin zone, as inferred by quasiparticle wave functions in the conduction and valence bands which are strongly localized in separate layers. However, moderate fields produce charge densities which are distributed across both layers. In this case, hybrid ILE and intralayer exciton states come into play, while the e-h overlaps and, consequently, exciton binding energies and oscillator strengths are significantly enhanced. The possibility of tuning the exciton binding energy and its PL emission intensity using an applied field opens an interesting avenue towards the search and enhancement of ILE exciton states, whose experimental observation has proved to be elusive.

Acknowledgments. Discussions with J. Kunstman, D. R. Reichman, and C. W. Wong are gratefully acknowledged. A.C. has been financially supported by CNPq, through the PRONEX/FUNCAP and PQ programs. J.A. and T.L. acknowledge support from NSF ECCS-1542202. We acknowledge computational support from the Minnesota Supercomputing Institute (MSI).

[1] K. F. Mak, C. Lee, J. Hone, J. Shan, and T. F. Heinz, Phys. Rev. Lett. **105**, 136805 (2010).

[2] R. Ganatra and Q. Zhang, ACS Nano **8**, 4074 (2014).

[3] Y. Sun, D. Wang, and Z. Shuai, J. Phys. Chem. C **120**, 21866 (2016).

[4] Y. Zhang, T.-R. Chang, B. Zhou, Y.-T. Cui, H. Yan, Z. Liu, F. Schmitt, J. Lee, R. Moore, Y. Chen, H. Lin, H.-T. Jeng, S.-K. Mo, Z. Hussain, A. Bansil, and Z.-X. Shen, Nat. Nanotechnol. **9**, 111 (2014).

[5] J. K. Ellis, M. J. Lucero, and G. E. Scuseria, Appl. Phys. Lett. **99**, 261908 (2011).

[6] T. Cheiwchanchamnangij and W. R. L. Lambrecht, Phys. Rev. B **85**, 205302 (2012).

[7] A. Kumar and P. K. Ahluwalia, Eur. Phys. J. B **85**, 186 (2012).

[8] *2D Materials*, edited by P. Avouris, T. F. Heinz, and T. Low (Cambridge University Press, Cambridge, U.K., 2017).

[9] T. Low, A. Chaves, J. D. Caldwell, A. Kumar, N. X. Fang, P. Avouris, T. F. Heinz, F. Guinea, L. Martin-Moreno, and F. Koppens, Nat. Mater. **16**, 182 (2017).

[10] Z. Ye, T. Cao, K. O'Brien, H. Zhu, X. Yin, Y. Wang, S. G. Louie, and X. Zhang, Nature (London) **513**, 214 (2014).

[11] B. Zhu, X. Chen, and X. Cui, Sci. Rep. **5**, 9218 (2015).

[12] M. M. Ugeda, A. J. Bradley, S.-F. Shi, F. H. da Jornada, Y. Zhang, D. Y. Qiu, W. Ruan, S.-K. Mo, Z. Hussain, Z.-X. Shen, F. Wang, S. G. Louie, and M. F. Crommie, Nat. Mater. **13**, 1091 (2014).

[13] S. Tongay, H. Sahin, C. Ko, A. Luce, W. Fan, K. Liu, J. Zhou, Y.-S. Huang, C.-H. Ho, J. Yan, D. F. Ogletree, S. Aloni, J. Ji, S. Li, J. Li, F. M. Peeters, and J. Wu, Nat. Commun. **5**, 3252 (2014).

[14] O. B. Aslan, D. A. Chenet, A. M. van der Zande, J. C. Hone, and T. F. Heinz, ACS Photonics **3**, 96 (2016).

[15] A. Chernikov, T. C. Berkelbach, H. M. Hill, A. Rigosi, Y. Li, O. B. Aslan, D. R. Reichman, M. S. Hybertsen, and T. F. Heinz, Phys. Rev. Lett. **113**, 076802 (2014).

[16] K. He, N. Kumar, L. Zhao, Z. Wang, K. F. Mak, H. Zhao, and J. Shan, Phys. Rev. Lett. **113**, 026803 (2014).

[17] E. J. Sie, A. J. Frenzel, Y.-H. Lee, J. Kong, and N. Gedik, Phys. Rev. B **92**, 125417 (2015).

[18] J. S. Ross *et al.*, Nat. Commun. **4**, 1474 (2012).

[19] G. Wang, X. Marie, I. Gerber, T. Amand, D. Lagarde, L. Bouet, M. Vidal, A. Balocchi, and B. Urbaszek, Phys. Rev. Lett. **114**, 097403 (2015).

[20] B. Miller, A. Steinhoff, B. Pano, J. Klein, F. Jahnke, A. Holleitner, and U. Wurstbauer, Nano Lett. **17**, 5229 (2017).

[21] P. Rivera, J. R. Schaibley, A. M. Jones, J. S. Ross, S. Wu, G. Aivazian, P. Klement, K. Seyler, G. Clark, N. J. Ghimire, J. Yan, D. G. Mandrus, W. Yao, and X. Xu, Nat. Commun. **6**, 6242 (2015).

[22] A. F. Rigosi, H. M. Hill, Y. Li, A. Chernikov, and T. F. Heinz, Nano Lett. **15**, 5033 (2015).

[23] H. Fang, C. Battaglia, C. Carraro, S. Nemsak, B. Ozdol, J. S. Kang, H. A. Bechtel, S. B. Desai, F. Kronast, A. A. Unal, G. Conti, C. Conlon, G. K. Palsson, M. C. Martin, A. M. Minor, C. S. Fadley, E. Yablonovitch, R. Maboudian, and A. Javey, Proc. Natl. Acad. Sci. USA **111**, 6198 (2014).

[24] Y. Gong, S. Lei, G. Ye, B. Li, Y. He, K. Keyshar, X. Zhang, Q. Wang, J. Lou, Z. Liu, R. Vajtai, W. Zhou, and P. M. Ajayan, Nano Lett. **15**, 6135 (2015).

[25] Y.-C. Lin, R. K. Ghosh, R. Addou, N. Lu, S. M. Eichfeld, H. Zhu, M.-Y. Li, X. Peng, M. J. Kim, L.-J. Li, R. M. Wallace, S. Datta, and J. A. Robinson, Nat. Commun. **6**, 7311 (2015).

[26] S. Pak, J. Lee, Y.-W. Lee, A.-R. Jang, S. Ahn, K. Y. Ma, Y. Cho, J. Hong, S. Lee, H. Y. Jeong, H. Im, H. S. Shin, S. M. Morris, S. Cha, J. I. Sohn, and J. M. Kim, Nano Lett. **17**, 5634 (2017).

[27] V. O. Özçelik, J. G. Azadani, C. Yang, S. J. Koester, and T. Low, Phys. Rev. B **94**, 035125 (2016).

[28] C.-H. Lee, G.-H. Lee, A. M. van der Zande, W. Chen, Y. Li, M. Han, X. Cui, G. Arefe, C. Nuckolls, T. F. Heinz, J. Guo, J. Hone, and P. Kim, Nat. Nanotechnol. **9**, 676 (2014).

[29] T. C. Berkelbach, M. S. Hybertsen, and D. R. Reichman, Phys. Rev. B **88**, 045318 (2013).

[30] S. Latini, T. Olsen, and K. S. Thygesen, Phys. Rev. B **92**, 245123 (2015).

[31] G. Kresse and J. Furthmuller, Phys. Rev. B **54**, 11169 (1996).

[32] P. E. Blochl, Phys. Rev. B **50**, 17953 (1994).

[33] J. P. Perdew, K. Burke, and M. Ernzerhof, Phys. Rev. Lett. **77**, 3865 (1996).

[34] S. Grimme, J. Comput. Chem. **27**, 1787 (2006).

[35] G. Makov and M. C. Payne, Phys. Rev. B **51**, 4014 (1995).

[36] R. M. Feenstra, N. Srivastava, Q. Gao, M. Widom, B. Diaconescu, T. Ohta, G. L. Kellogg, J. T. Robinson, and I. V. Vlassiouk, Phys. Rev. B **87**, 041406(R) (2013).

[37] See Supplemental Material at http://link.aps.org/supplemental/10.1103/PhysRevB.98.121302 for a detailed description of the exciton model, including a list of parameters and effective masses used in our calculations.

[38] L. Banyai, I. Galbraith, C. Ell, and H. Haug, Phys. Rev. B **36**, 6099 (1987).

[39] Z. Jin, X. Li, J. T. Mullen, and K. W. Kim, Phys. Rev. B **90**, 045422 (2014).

[40] F. A. Rasmussen and K. S. Thygesen, J. Phys. Chem. C **119**, 13169 (2015).

[41] K. Andersen, S. Latini, and K. Thygesen, Nano Lett. **15**, 4616 (2015).

[42] L. S. R. Cavalcante, A. Chaves, B. Van Duppen, F. M. Peeters, and D. R. Reichman, Phys. Rev. B **97**, 125427 (2018).

[43] D. Huang and E. Kaxiras, Phys. Rev. B **94**, 241303(R) (2016).

[44] J. Kunstmann, F. Mooshammer, P. Nagler, A. Chaves, F. Stein, N. Paradiso, G. Plechinger, C. Strunk, C. Schüller, G. Seifert, D. R. Reichman, and T. Korn, Nat. Phys. **14**, 801 (2018).

[45] A. T. Hanbicki, H.-J. Chuang, M. R. Rosenberger, C. S. Hellberg, S. V. Sivaram, K. M. McCreary, I. I. Mazin, and B. T. Jonker, ACS Nano **12**, 4719 (2018).

[46] A. Ciarrocchi, D. Unuchek, A. Avsar, K. Watanabe, T. Taniguchi, and A. Kis, arXiv:1803.06405.

[47] R. J. Elliott, Phys. Rev. **108**, 1384 (1957).

[48] H. Yu, Y. Wang, Q. Tong, X. Xu, and W. Yao, Phys. Rev. Lett. **115**, 187002 (2015).

[49] F. Wu, T. Lovorn, and A. H. MacDonald, Phys. Rev. B **97**, 035306 (2018).

[50] B. Szafran, E. Barczyk, F. M. Peeters, and S. Bednarek, Phys. Rev. B **77**, 115441 (2008).

[51] K. Nishi and T. Hiroshima, Appl. Phys. Lett. **51**, 320 (1987).

[52] S. R. Andrews, C. M. Murray, R. A. Davies, and T. M. Kerr, Phys. Rev. B **37**, 8198 (1988).